Progress in Medical Devices
ISSN: 2957-5478

Zentime

Research Article https://doi.org/10.61189/389587wfmupp

A novel instrument guidance device for enhanced surgical navigation

Xuelong Wang[1], Changjiang Zhou[2], Zhenyi Huang[2], Hao Zhao[2], Shiju Yan[1]

[1]School of Health Science and Engineering, University of Shanghai for Science and Technology, Shanghai 200093, China. [2]Department of Ultrasound, Jinan City People's Hospital, People's Hospital Affiliated to Shandong First Medical University, Jinan 250000, Shandong Province, China.

Corresponding author: Changjiang Zhou.

Declaration of conflict of interest: None.

Received September 28, 2024; Accepted December 16, 2024; Published June 30, 2025

Highlights

- A compact instrument guidance device for minimally invasive surgery was developed, capable of real-time monitoring of angle and key status.
- The device provides navigation information and estimates the lesion depth, aiding in preoperative planning.

Abstract

Objectives: The key to an ultrasound-guided system is to accurately determine the spatial position of the surgical instrument. The size and shape of the optical positioning target in the optical positioning device can restrict the doctor's hand movements. Additionally, the use of a binocular camera occupies valuable operating room space. To reduce both the space occupation and the impact on surgical procedures, this paper presents a device designed to provide enhanced navigation information to assist the surgeon. **Methods:** The proposed device is equipped with an angle sensor and a button. The angle sensor measures the relative angle between the puncture device and the ultrasound probe in real time. The button assists the surgeon in measuring the depth of the surgical target before performing the puncture. Furthermore, we propose a filtering algorithm to reduce noise in the angle sensor's output signal. The device's performance was evaluated using an ultrasound instrument and an experimental setup for data collection and testing. **Results:** The filtering algorithm effectively reduced noise in the angular data. After filtering, the Signal Smoothness decreased from 0.036989 to 0.0010376, the Coefficient of Variation decreased from 0.00046682 to 0.0004323, and the Count of Local Extrema decreased from 251 to 135. Additionally, we collected and compared the coordinates of the guide line endpoints at the tip of the puncture needle and found an average point-to-point error of 3.53 pixel. **Conclusions:** The developed guidance device and filtering algorithm provide valuable navigation data, supporting the surgeon's operations.

Keywords: Ultrasound surgical navigation, filtering algorithm, minimally invasive surgery, angle sensor

Introduction

Minimally invasive techniques have become a mainstream approach in modern surgery due to their advantages of less trauma and faster recovery. These techniques are widely used in various clinical fields, including thoracic surgery, eye surgery, orthopedic surgery, abdominal surgery, neurosurgery, and obstetric and gynecological surgery [1-4]. Ultrasound guidance plays a crucial role in minimally invasive surgery by providing real-time navigation information, reducing physician fatigue, and improving surgical success rates. Studies have shown that ultrasound-guided techniques result in higher success rates in peripheral venous catheter insertion [5-7]. Pavone et al. showed that ultrasound-guided robotic surgery can shorten the duration of minimally invasive procedures [8]. Liang et al. found that ultrasound-guided acupotomy for trigger finger significantly increased the surgical success rate while reducing recurrence and complication rates compared to the traditional approach [9].

The core function of an ultrasound guidance system is to accurately determine the spatial position of surgical instruments and provide

Address correspondence to: Changjiang Zhou, Department of Ultrasound, Jinan City People's Hospital, No. 001 Xuehu Street, Jinan 250000, Shandong Province, China. Tel: +86-18956153985. E-mail: yanshiju@usst.edu.cn.

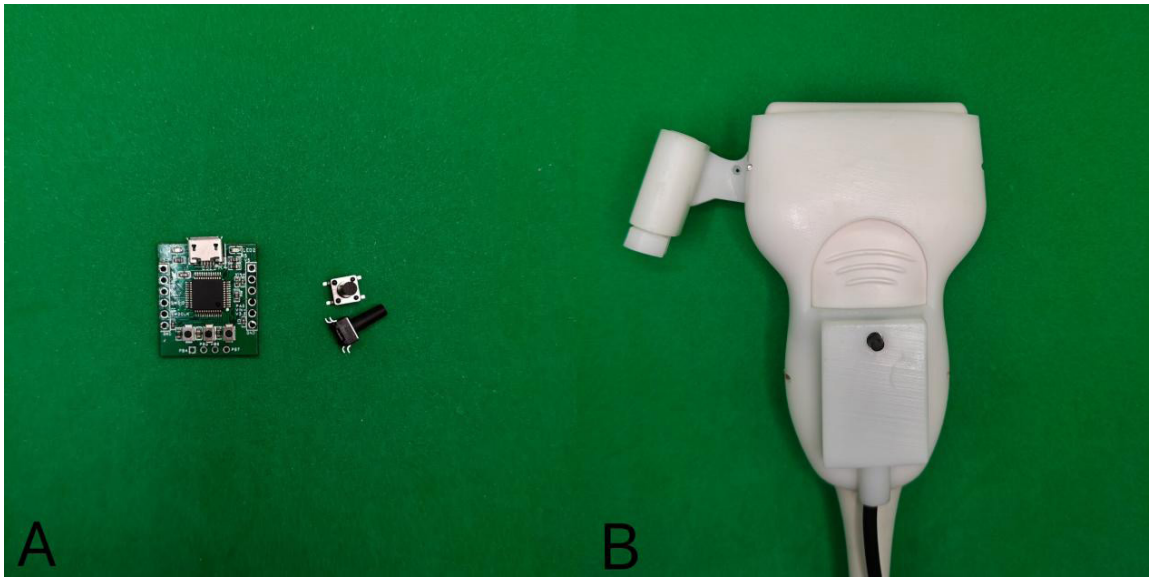

Figure 1. Circuit Board, Buttons and Instrument Guide Device. (A) Independently designed circuit board and button; (B) 3D printed and installed instrument guidance device.

navigation information to the surgeon. One commonly used method is optical localization-assisted technology, which involves placing optical tracking targets on both the ultrasound probe and surgical instruments, with binocular cameras positioned in the operating room [10-13]. The size and shape of the optical tracking sensor directly influence the surgeon's hand movements, and the presence of binocular camera occupies valuable space in the operating room. These factors can impact the efficiency and ease of surgery.

To reduce space occupation and minimize interference with the surgeon's operations, various small-scale surgical guidance techniques have been developed. Golafsoun et al. developed an MR-UIG system for central line procedures, which uses a six-degree-of-freedom transducer to track the spatial position of the ultrasound probe [14]. Minchev et al. designed a micro-robotic guidance device and tested it in 150 stereotactic procedures [15]. In this paper, we present a mechatronics-based instrument guidance device that provides navigation information to the surgeon. The device includes an angle sensor for real-time measurement of the relative angle between the puncture device and the ultrasound probe, and a keypad for assisting the surgeon in virtually measuring the depth of the surgical target before performing the puncture. We have designed the instrument to be compact and easy to hold, minimizing the impact on the surgeon's hand movements and reducing space occupation. Additionally, we propose a filtering algorithm to reduce noise in the sensor data.

Design and realization of instrument guidance device

Structural design of instrument guidance device

In this study, we designed a novel instrument guidance device for surgical navigation. The device is compact, easy to hold, and capable of obtaining precise angles for surgical instruments. It also assists the surgeon in virtually measuring the depth of the surgical target prior to puncture.

The device consists of an upper and lower casing, which are fixed together using screws and nuts. The lower casing has a pocket for the angle sensor, with a perforated design to allow the puncture guide to be mounted on the rotation axis of the angle sensor. The puncture guide transmits angle change to the sensor, enabling precise measurement of the relative angle between the puncture device and the ultrasound probe. This angle data is then used by the ultrasound navigation system to provide real-time visual guidance for the surgeon.

The upper casing includes grooves to house the sensor drive circuit board and a depth measurement button, as shown in **Figure 1A**. The button opening is located below the circuit board casing, allowing the surgeon to press it after determining the puncture angle to measure the depth of the surgical target. The virtual depth information obtained from this measurement aids in preoperative planning.

Additionally, we designed a puncture guide

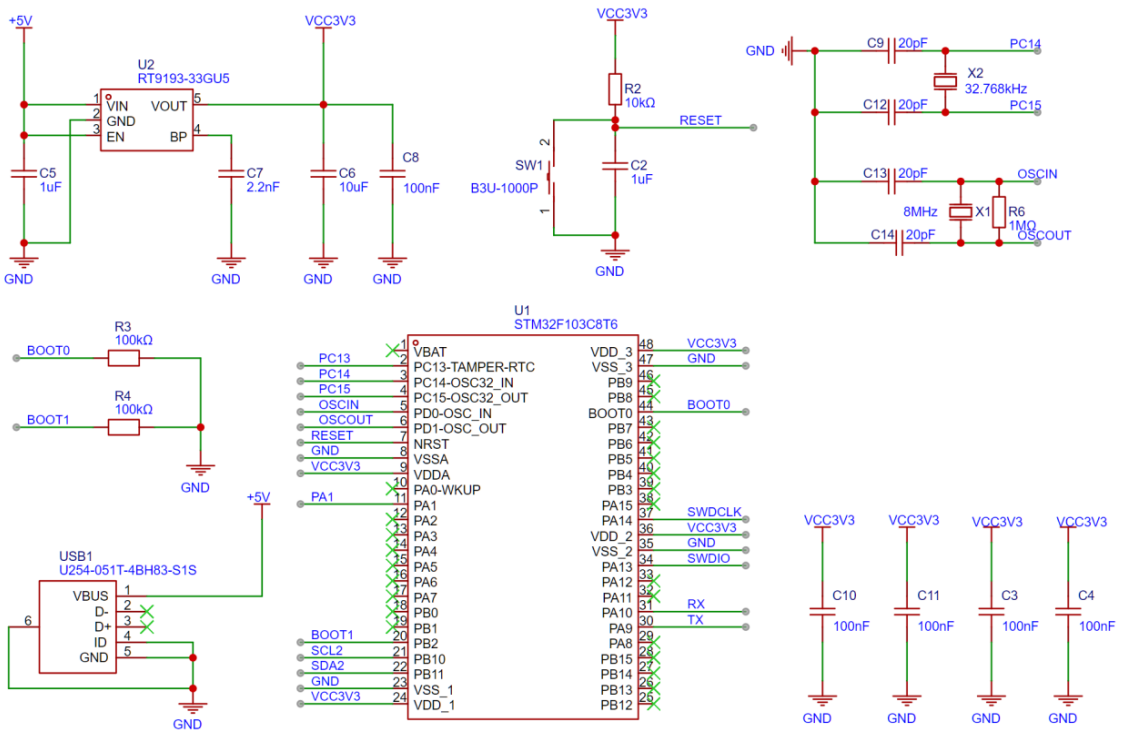

Figure 2. Schematic Diagram.

sleeve that accommodates puncture needles of varying sizes. The sleeve consists of an outer and an inner cylinder. A sensor fixing column at the lower part of the outer cylinder transmits the relative angle between the puncture guide sleeve and the ultrasound probe to the angle sensor. The inner cylinder has three different inner groove sizes to accommodate three different puncture needles. Finally, the design is realized by 3D printing and shown in **Figure 1B**.

Hardware design of the sensor drive module

The main function of the angle sensor drive module is to collect angle data and key status signals. The main controller of this module is STM32F103C8T6, which is sufficiently powerful to run the data acquisition and filtering algorithm designed for this project. The main control chip circuit is shown in **Figure 2**.

The STM32F103C8T6 microcontroller includes two built-in 12-bit analog-to-digital converters (ADC) that can be used for external analog signal acquisition. However, to enhance detection accuracy and provide more accurate navigation information, we have integrated an external 16-bit high-precision ADC chip, the ADS1110. This ADC chip features a built-in gain amplifier and supports four common sampling rates: 15SPS, 30SPS, 60SPS, and 240SPS.

The ADS1110 uses differential signal input pins (VIN+ and VIN-). It supports two acquisition modes: bipolar differential signal acquisition and single-ended acquisition. In this project, the single-ended acquisition mode is employed, with VIN- grounded and the input signal connected to VIN+. The single-ended signal range is from 0 V to 2.048 V.

For ADC chips, the conversion of input analog voltage to a digital value is governed by the following formula for an N-bit ADC:

$$Value = (\frac{V_{out}}{V_{ref}}) \times (2^N - 1) \quad (1 - 1)$$

Where: Value is the digital output from the ADC, V_{out} is the analog output voltage of the potentiometer, V_{ref} is the reference voltage for ADC (2.048 V in this case), and N is the ADC resolution (16 bits in this project).

This project uses the RDC501051A angle sensor to obtain the relative angle between the the surgical puncture instrument and the ultrasound probe. The RDC501051A is a resistive position sensor known for its compact design and high accuracy. The linear relationship between the displacement of this sensor and its output voltage value is suitable for this project. The sensor has a resistance of 10 kΩ and a linearity accuracy of ± 2%. The position of the wiper of this potentiometer is linearly related to the output analog voltage, described by the following formula:

$$V_{out} = V_{CC} \times (\frac{P}{P_{max}}) \quad (1 - 2)$$

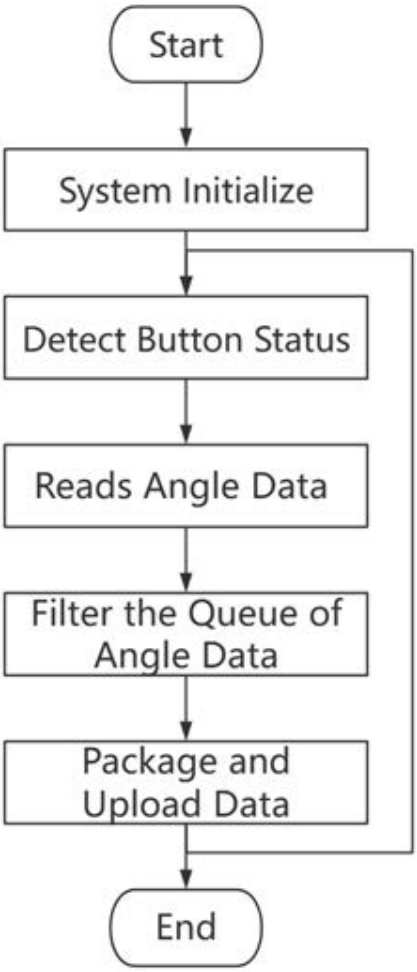

Figure 3. Software Design Process Flowchart.

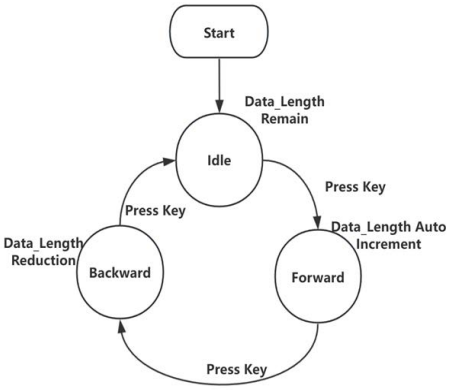

Figure 4. State Transition Diagram.

Where, V_{cc} is the specified value (2.048 V), P is the current position of the potentiometer wiper, and $Pmax$ is the maximum position of the potentiometer. When the wiper is at the starting position (P=0), the output voltage is 0 V. When the wiper is at the end position (P= $Pmax$), the output voltage is V_{cc}.

Software design of sensor drive modules

The angle sensor driver module is responsible for collecting and transmitting angle data and key status signals. The software program flowchart of this module is shown below in **Figure 3**.

The software follows a cyclic structure. After initializing each module, the chip continuously detects button status and angle data, and the filtered angle data and button status are then packaged and sent to the host computer. A key part to the software algorithm is filtering the angle data to eliminate outliers and minimize the impact of noise.

Noise is a common issue in data acquisition systems caused by various factors, such as electromagnetic interference, mechanical vibrations, motion artifacts, and imprecise circuit design [16-18]. This noise can affect the linearity of sensor and distort statistical properties, complicating accurate data analysis [19]. Signal-to-noise separation is a fundamental challenge in biological and data acquisition systems [20]. This project uses two approaches to filter and reduce noise: hardware circuit improvements and software filtering algorithms.

Hardware approach: A filter capacitor is connected between the sampling input pin and ground of the ADC chip. This capacitor can effectively filter high-frequency noise, improving the stability and accuracy of the ADC's signal conversion.

Software approach: Based on the observation of continuous static data waveforms, we identified the noise as impulse noise and Gaussian noise. The software filtering algorithm is divided into two parts: Part one, the angle detection driver module removes the maximum and minimum values from ten consecutive data points, then calculates the mean value; Part two, The host computer applies the standard deviation method to remove outliers from 100 consecutive data points, followed by mean filtering with a window size of 10. The standard deviation method used to filter impulse noise is calculated using the following formula:

$$s = \sqrt{\frac{\sum_{i=1}^{n}(x_i - \bar{x})}{n-1}} \quad (1\text{-}3)$$

Where, s is the sample standard deviation, n is the number of data points in the sample, x_i is each individual data point, and $\bar{x}$ is the mean of the sample. The denominator uses n-l instead of n, which is known as degrees of freedom correction to provide an unbiased estimate of the population standard deviation.

In the board-level filtering process, we compute the mean $\bar{x}$ and standard deviation. If a data point exceeds the mean plus or minus three times, the data is determined to be outlier. The remaining data are then subjected to mean filtering to produce the final filtered result.

Depth measurement algorithm design

In response to feedback from the doctor, we designed a depth measurement function to aid in pre-surgical planning. This function allows the doctor to estimate the surgical target's penetration depth after determining the puncture angle, facilitating better surgical preparation.

A user button (model SW-6 mm) is added to the sensor driver module, see **Figure 1A**, enabling the doctor to adjust the depth measurement. The algorithm cycles between idle, forward, and backward states, with each state transition triggering a corresponding action, as shown in **Figure 4**. Pressing the button changes the user state, allowing for the adjustment of the depth measurement line in both forward and backward directions.

In the algorithm, we define a depth value, L_d (length of data), which is the modal length of the depth measurement line. This value increases when the button is pressed to enter "forward" mode and decreases for the "backward" mode. Importantly, this value is not the actual physical world penetration depth. To establish the relationship between L_d and the true puncture depth, we conducted data acquisition for 110 points. At each point, we measured the actual depth and performed polynomial fitting to obtain the following equation:

$$y = P_1 \times L_d + P_2$$
$$\begin{cases} P_1 = 16.32 \\ P_2 = -1.074 \end{cases} \quad (1 - 4)$$

Where x is the depth value L_d and y is the physical real puncture depth.

Based on the above equation, we derived the relationship between the physical puncture depth and the pixel coordinates in the ultrasound image:

$$y = P_1 \times \sqrt{(P_x + P_y)^2} + P_2 \quad (1 - 5)$$

Where P_x and P_y are the pixel coordinates on the ultrasound image. The above formulas and algorithms were implemented on the host computer to enable the depth measurement function.

Results

We used a variety of data metrics to measure the performance of the devices and algorithms.

Signal Smoothness measures the degree of fluctuation and smoothness in the signal. It was assessed using the first and second derivatives:

$$S_1 = \frac{1}{N-1}\sum_{i=1}^{N-1} |y_{i+1} - y_i| \quad (2 - 1)$$

$$S_2 = \frac{1}{N-1}\sum_{i=1}^{N-2} |y_{i+2} - 2y_{i+1} + y_i| \quad (2 - 2)$$

Where y_i is the signal value at point i, and n is the total number of points, and S_1 and S_2 are its first-order and second-order derivatives.

The Coefficient of Variation (CV) measures the dispersion of the data relative to its mean. A lower CV indicates less data volatility:

$$CV = \frac{\sigma}{\mu} \times 100\% \quad (2 - 3)$$

Where σ is the standard deviation and μ is the mean of the data.

Count of Local Extrema counts the number of local maxima and minima in the filtered data. A reduction in local extrema indicates fewer sharp changes:

For each point, compare it to its neighboring points;

If a point is greater than its neighboring, it is a local maximum;

If a point is smaller than its neighbors, it is a local minimum;

The total number of local maxima and minima is then calculated.

Root Mean Square Error (RMSE) measures the magnitude of the error between the predicted values and the actual observed values:

$$RMSE = \sqrt{\frac{1}{n}\sum_{i=1}^{n}(y_i - \hat{y}_i)^2} \quad (2 - 4)$$

Where y_i is the true value and $\hat{y}_i$ is the predicted value for the i-th data point.

Mean Absolute Error (MAE) measures average absolute error between the predicted and actual values:

$$MAE = \frac{1}{n}\sum_{i=1}^{n} |y_i - \hat{y}_i| \quad (2 - 5)$$

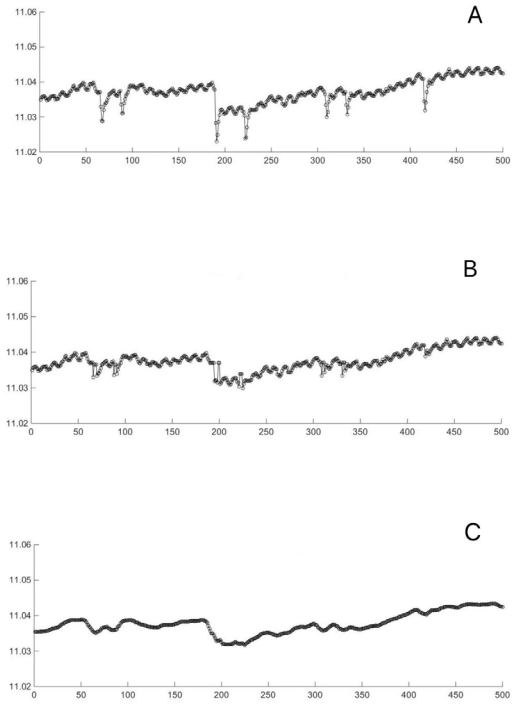

Figure 5. Filter algorithm result data. (A) Raw data; (B) Intermediate results; (C) Filtered results.

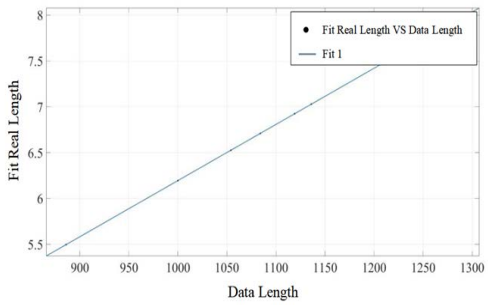

Figure 6. Fitting Function and Fitted Data Points.

Where y_i is the true value and $\hat{y}_i$ is the predicted value for the i-th data point.

The R-squared value indicates the proportion of variance in the dependent variable explained by the independent variables in the regression model. A value closer to 1 indicates better explanatory power:

$$R^2 = 1 - \frac{SSE}{SST} \quad (2 - 6)$$

Where, SSE (Sum of Squares Errors) stands for the sum of squared residuals, which is the differences between the observed and predicted values. SST (Sum of Squares Total) stands for sum of squares total, which is the sum of squared differences between each observation and the overall mean.

Experimental results of filtering algorithm

The angle acquisition module was kept stationary, and 1,000 data points were collected to reflect the fluctuations caused by the instrument's inherent noise, with no external interference. Afterwards, the designed filtering algorithm was then applied to the data to obtain the result data.

The pre-filtered and post-filtered data are shown in **Figure 5**. **Figure 5A** shows the original data before filtering; **Figure 5B** shows the intermediate results after filtering using the standard deviation method with outlier data removed; **Figure 5C** shows the final filtered results after applying both the standard deviation method and mean filtering, with outliers and random noise removed.

As shown in the figures, the standard deviation method effectively filters out the transient impulse noise in the original data, while mean filtering removes random noise, resulting in smoother data. To evaluate the effectiveness of the filtering algorithm, we applied the performance index tests mentioned earlier to the data before and after filtering. The results of the performance metrics are summarized in **Table 1**.

The Signal Smoothness significantly improved, decreasing from 0.036989 to 0.0010376, the CV decreased from 0.00046682 to 0.0004323, and the Count of Local Extrema decreased from 251 to 135. These improvements suggest that the filtering algorithm enhances the accuracy and stability of angle data acquisition. The reduction in extreme values and peaks further indicates that the filtered data are more stable.

Depth measurement algorithm test results

To establish the relationship between the depth measurement value L_d and the actual penetration depth, we utilized MATLAB's polynomial fitting tool to generate a fitting formula. The formula, along with the fitted data points, is shown as **Figure 6**.

The results demonstrate a unitary function correspondence between L_d and true depth. The performance metrics of the fitted function are presented in the **Table 2**.

The coefficient of determination of the fitting formula is 1, and the RMSE and SSE values are extremely small, which indicates that the fitting formula has strong explanatory power and can

Table 1. Performance metrics of raw data, intermediate results and filtered results

	Signal Smoothness	CV	Count of Local Extrema
Raw data	0.03698900	0.00046682	251
Intermediate results	0.02928600	0.00044010	291
Filtered results	0.00103760	0.00043230	135

Note: CV, Coefficient of Variation.

Table 2. Performance parameters for fitting functions

SSE	R-squared	RMSE
5.9875e-28	1	2.1218e-15

Note: SSE, Sum of Squared Errors; RMSE, Root Mean Square Error.

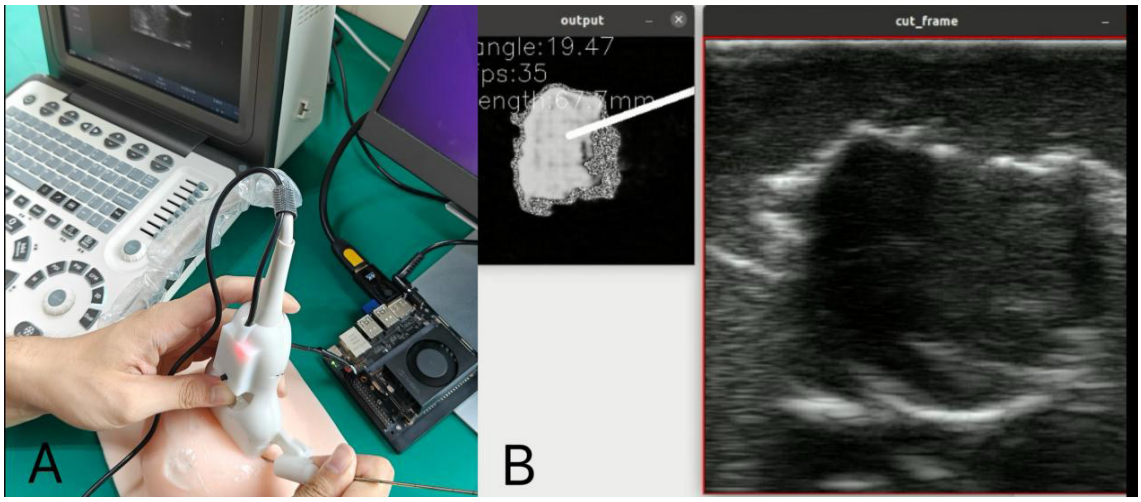

Figure 7. Experimental Bench and Experimental Effect. (A) Experimental Bench; (B) Upper Computer Operation Effect.

accurately describe the relationship between L_d and the real depth in the physical world.

We then developed a test program that used an image processing algorithm to measure the pixel coordinates of the puncture needle tip in the ultrasound image. The algorithm then compared these pixel coordinates with those of the guide-line endpoint, calculating the error to assess the performance.

In the tests, we collected coordinate data from 150 pairs of points. The average error between points was 3.53 pixels. Using the fitting formula, the corresponding average error for the depth measurement algorithm was found to be 0.216 mm. Finally, we constructed an experimental bench and performed simulation testing using the puncture needle with scale, ferrule, breast body model, ultrasound instrument, and probe fixation bracket designed in this paper. The set-up and test results are shown in the **Figure 7**. The upper computer running results show that the angle at the center of the lesion is 19.47 degrees, with a calculated virtual depth of 67.7 mm.

Discussion

In this paper, an instrument guidance device capable of providing navigation information is presented. During the design process, several iterations were performed to optimize both the hand-holding sensation and device's size, resulting in a compact, user-friendly version.

We developed a filtering algorithm that processes data from the ADS1110 chip to provide accurate angle information to the physician. The filtered data meets the required accuracy and smoothness, with reduced noise. Further optimizations can be made at both the hardware and software levels. On the hardware side, adding an RC filter circuit could further reduce noise. On the software side, increasing the sampling rate to 240 sps could improve the real-time response speed and enhance the data volume, ensuring a faster and more responsive system.

To assist the surgeon in estimating the puncture depth before the procedure, we introduced a virtual guide-line feature. This feature has shown strong performance, but it can also be

optimized further. Hardware improvements, such as incorporating a magnetic sensor for real-time depth measurement, could increase accuracy. On the software side, implementing a tip detection algorithm would allow for more precise real-time depth calculations.

Additionally, we developed an angular depth measurement algorithm tailored to the doctor's needs. This algorithm aids in preoperative planning by estimating the puncture depth using intraoperative imaging. The final test results demonstrate that the virtual bathymetry algorithm we designed performs well and meets the expected accuracy and reliability.

Conclusions

In this paper, we present an instrument guidance device that provides real-time navigation information to assist physicians during procedures. The device's mechanical structure was carefully engineered and 3D printed. An angle sensor, capable of measuring angle between the puncture device and the ultrasound probe, is integrated into the design. A sensor driver module drives the angle sensor and capture real-time keystroke information. We also developed a filtering algorithm to reduce noisy in the angle sensor data and a depth measurement algorithm to estimate the virtual depth before puncture.

The filtering algorithm effectively addresses the noise characteristics of the sensor data, ensuring accurate angle navigation for the physician. The depth measurement algorithm is precise in both positioning and measurement, helping doctors determine the accurate depth of the surgical target prior to surgery.

The instrument guidance device is compact, lightweight, and easy for the doctor to hold, without interfering with hand movements during the procedure. Data collected using an ultrasound instrument and experimental bench validated the performance of the algorithms. The results confirm that the device provides accurate and reliable navigation data to assist physicians in their procedures.

Author Contributions: Shiju Yan, as the leader of the project, formulated the detailed project plan, coordinated the resources of all parties, and comprehensively coordinated the planning and promotion of the project. Xuelong Wang is responsible for the design of the device structure, circuit board design, algorithm design and thesis writing. Changjiang Zhou is the co-corresponding author of the paper. He is responsible for researching the background of the project, planning and conceptualizing the paper, and providing suggestions and thoughts from clinical experience and doctors' perspectives. Zhenyi Huang was responsible for the assembly and testing of the device structure, as well as the operation of the device to collect a large amount of data. Hao Zhao assisted Zhenyi Huang in data collection and performance testing of the filtering algorithm and the device designed in this paper.

References

[1] Balafoutas D, Vlahos N. The role of minimally invasive surgery in gynaecological cancer: an overview of current trends. Facts Views Vis Obgyn 2024;16(1):23-33.

[2] Ditonno F, Franco A, Manfredi C, et al. Trends and Costs of Minimally Invasive Surgery for Kidney Cancer in the US: A Population-based Study. Urology 2024;189:41-48.

[3] Li R, Liu H, Zhang K, et al. Global tendency and research trends of minimally invasive surgery for glaucoma from 1992 to 2023: A visual bibliometric analysis. Heliyon 2024;10(16):e36591.

[4] Sang D, Guo J, Meng H, et al. Global Trends and Hotspots of Minimally Invasive Surgery in Lumbar Spinal Stenosis: A Bibliometric Analysis. J Pain Res 2024;17:117-132.

[5] Doniger SJ, Ishimine P, Fox JC, et al. Randomized controlled trial of ultrasound-guided peripheral intravenous catheter placement versus traditional techniques in difficult-access pediatric patients. Pediatr Emerg Care 2009;25(3):154-159.

[6] Skulec R, Callerova J, Vojtisek P, et al. Two different techniques of ultrasound-guided peripheral venous catheter placement versus the traditional approach in the pre-hospital emergency setting: a randomized study. Intern Emerg Med 2020;15(2):303-310.

[7] Otani T, Morikawa Y, Hayakawa I, et al. Ultrasound-guided peripheral intravenous access placement for children in the emergency department. Eur J Pediatr 2018;177(10):1443-1449.

[8] Pavone M, Seeliger B, Teodorico E, et al. Ultrasound-guided robotic surgical procedures: a systematic review. Surg Endosc 2024;38(5):2359-2370.

[9] Liang YS, Chen LY, Cui YY, et al. Ultrasound-guided acupotomy for trigger finger: a systematic review and meta-analysis. J Orthop Surg Res 2023;18(1):678.

[10] Xiao G, Bonmati E, Thompson S, et al. Electromagnetic tracking in image-guided laparoscopic surgery: Comparison with optical tracking and feasibility study of a combined

laparoscope and laparoscopic ultrasound system. Med Phys 2018;45(11):5094-5104.
[11] Yamada A, Tokuda J, Naka S, et al. Magnetic resonance and ultrasound image-guided navigation system using a needle manipulator. Med Phys 2020;47(3):850-858.
[12] Gao W, Jiang B, Kacher DF, et al. Real-time probe tracking using EM-optical sensor for MRI-guided cryoablation. Int J Med Robot 2018;14(1):10.1002/rcs.1871.
[13] Manni F, Elmi-Terander A, Burström G, et al. Towards Optical Imaging for Spine Tracking without Markers in Navigated Spine Surgery. Sensors (Basel) 2020;20(13):3641.
[14] Ameri G, Baxter JSH, Bainbridge D, et al. Mixed reality ultrasound guidance system: a case study in system development and a cautionary tale. Int J Comput Assist Radiol Surg 2018;13(4):495-505.
[15] Minchev G, Wurzer A, Ptacek W, et al. Development of a miniaturized robotic guidance device for stereotactic neurosurgery. J Neurosurg 2021;137(2):479-488.
[16] Liu J, Wang H, Kogos LC, et al. Optical spatial filtering with plasmonic directional image sensors. Opt Express 2022;30(16):29074-29087.
[17] Nathan V, Jafari R. Particle Filtering and Sensor Fusion for Robust Heart Rate Monitoring Using Wearable Sensors. IEEE J Biomed Health Inform 2018;22(6):1834-1846.
[18] Wang M, Li Z, Zhang Q, et al. Removal of Motion Artifacts in Photoplethysmograph Sensors during Intensive Exercise for Accurate Heart Rate Calculation Based on Frequency Estimation and Notch Filtering. Sensors (Basel) 2019;19(15):3312.
[19] Zhang Y, Wang R, Li S, et al. Temperature Sensor Denoising Algorithm Based on Curve Fitting and Compound Kalman Filtering. Sensors (Basel) 2020;20(7):1959.
[20] Taub M, Yovel Y. Segregating signal from noise through movement in echolocating bats. Sci Rep 2020;10(1):382.